Dichotomy in the Lithiation Pathway of Ellipsoidal and Platelet $LiFePO_4$ Particles Revealed through Nanoscale Operando State-of-Charge Imaging

*Yiyang Li, Johanna Nelson Weker, William E. Gent, David N. Mueller, Jongwoo Lim, Daniel A. Cogswell, Tolek Tyliszczak, and William C. Chueh**

$LiFePO_4$ is a promising phase-separating battery electrode and a model system for studying lithiation. The role of particle synthesis and the corresponding particle morphology on the nanoscale insertion and migration of Li is not well understood, and elucidating the intercalation pathway is crucial toward improving battery performance. A synchrotron operando liquid X-ray imaging platform is developed to track the migration of Li in $LiFePO_4$ electrodes with single-particle sensitivity. Lithiation is tracked in two particle types—ellipsoidal and platelet—while the particles cycle in an organic liquid electrolyte, and the results show a clear dichotomy in the intercalation pathway. The ellipsoidal particles intercalate sequentially, concentrating the current in a small number of actively intercalating particles. At the same cycling rate, platelet particles intercalate simultaneously, leading to a significantly more uniform current distribution. Assuming that the particles intercalate through a single-phase pathway, it is proposed that the two particle types exhibit different surface properties, a result of different synthesis procedures, which affect the surface reactivity of $LiFePO_4$. Alternatively, if the particles intercalate through nucleation and growth, the larger size of platelet particles may account for the dichotomy. Beyond providing particle engineering insights, the operando microscopy platform enables new opportunities for nanoscale chemical imaging of liquid-based electrochemical systems.

1. Introduction

$LiFePO_4$ is a promising positive electrode for Li-ion batteries (LIBs) and is a model phase-separating system.[1–5] The low Li ion and electron conductivities in $LiFePO_4$ generally require primary particle sizes in the hundreds of nanometers range.[6] Low-temperature synthesis routes, such as hydrothermal synthesis, have been used to control the size, shape, and morphology of $LiFePO_4$ particles.[7–11] Recently, interesting intercalation behaviors like particle-by-particle intercalation[12,13] and diamond-shaped lithiation cores[14–17] have been observed in $LiFePO_4$. However, little is understood about how different nanostructured particle morphologies, such as those of platelet,[7,11,18] rod,[19,20] and ellipsoidal[12,21] particles, affect these intercalation pathways, largely because these pathways cannot be probed by conventional electrochemical methods. Understanding the role of the particle synthesis on the lithiation pathway of $LiFePO_4$ will guide the design of battery particles to improve energy density, power density, and cycle life.

Recent advances in characterization methods have significantly improved the understanding of lithiation in $LiFePO_4$. Spatially averaged in situ X-ray diffraction has revealed the existence of metastable lithiation pathways,[22–24] such as solid solution.[24–26] High-resolution ex situ microscopy[12–16,27,28] has also been used to image the nanoscale state-of-charge (SOC) of single particles in partially charged

Y. Li, Dr. J. Nelson Weker, Dr. D. N. Mueller, Dr. J. Lim, Prof. W. C. Chueh
Department of Materials Science and Engineering
Stanford University
496 Lomita Mall, Stanford, CA 94305, USA
E-mail: wchueh@stanford.edu

Dr. J. Nelson Weker
Stanford Synchrotron Radiation Lightsource
SLAC National Accelerator Laboratory
2575 Sand Hill Road, Menlo Park, CA 94025, USA

W. E. Gent
Department of Chemistry
Stanford University
496 Lomita Mall, Stanford, CA 94305, USA

Dr. D. A. Cogswell
Samsung Advanced Institute of Technology
America, One Cambridge Center
STE #702, Cambridge, MA 02142, USA

Dr. T. Tyliszczak
Advanced Light Source
Lawrence Berkeley National Laboratory
One Cyclotron Road, Berkeley, CA 94720, USA

Prof. W. C. Chueh
Stanford Institute of Materials and Energy Sciences
SLAC National Accelerator Laboratory
2575 Sand Hill Road, Menlo Park, CA 94025, USA

DOI: 10.1002/adfm.201500286

electrodes. Such maps capture the equilibrium phase distribution within individual particles at a given Li concentration. It was recently shown that particles intercalate one-by-one at low cycling rates and that more particles intercalate simultaneously at higher rates of cycling.[13] However, relaxation effects in ex situ measurements preclude directly observing Li insertion and migration within individual particles, necessitating the use of in situ imaging.

In situ transmission electron microscopy (TEM) has been used to investigate lithiation of nanoparticles and nanowires at nanometer and Angstrom resolutions in real time,[29–34] typically under potentiostatic control. Complementary electron energy-loss spectroscopy has also revealed the nanoscale SOC distribution.[29,31–33] Strong beam-induced damage, however, has limited high-resolution SOC mapping to operando battery cells containing ionic liquid,[29] solid,[31] or aqueous[33] electrolytes. Such electrolytes have different interfacial and transport properties than the organic liquid electrolytes used in standard LIBs and likely change the lithiation pathway.

Recently, synchrotron-based transmission X-ray microscopy (TXM) operating in the hard X-ray regime (photon energy > 5000 eV) has emerged as a viable tool to image LIB chemistries in organic liquid electrolytes with low beam-induced damage.[35–42] The deep penetration of hard X-rays (tens of micrometers) enables TXM to probe the large volume expansion that accompanies micrometer-sized conversion[36,37,41] and alloying[38] electrodes, typically in modified coin or pouch cells. In conjunction with X-ray absorption spectroscopy, 2D TXM reveals the oxidation state of transition-metal cations in intercalation electrodes.[39,42] The long probing length of hard X-rays, however, makes it difficult to probe unagglomerated particles thinner than 500 nm. For example, a 200 nm thick $LiFePO_4$ particle absorbs ≈1% of the incident X-rays at the Fe K absorption edge.[43,44] In preliminary ex situ TXM experiments, we were unable to attain quantitative, single-particle X-ray absorption spectra from ≈200 nm thick nanoparticles.

Soft X-rays (photon energy < 2000 eV), in contrast to hard X-rays, have a short penetration length in the hundreds of nanometers,[43,44] making them ideally suited for probing lithiation in individual $LiFePO_4$ particles. A 200 nm thick $LiFePO_4$ particle absorbs ≈60% of the incident X-rays at the Fe L edge.[43,44] Soft X-ray scanning transmission X-ray microscopy has been used to study cross-sectioned electrodes and isolated $LiFePO_4$ particles ex situ at ≈25 nm resolution.[12–15] To carry out operando transmission microscopy experiments, however, the short penetration length of soft X-rays necessitates an in-plane electrochemical cell with a submicrometer-thick liquid electrolyte, such as the microfluidic cells used in liquid TEM experiments.[32,33] Construction of these miniaturized cells is significantly more challenging than the cells used in hard X-ray microscopy.

In addressing these challenges, we developed an operando liquid fluorescence-yield X-ray microscopy (FY-XRM) platform, operating in the soft X-ray regime, to dynamically track Li migration in $LiFePO_4$ electrodes cycling in an organic electrolyte. By detecting the fluorescent X-rays in a reflection geometry (**Figure 1**a,b), we overcome the challenges associated with transmission microscopy in the hard X-ray regime (low contrast for individual nanoparticles) and in the soft X-ray regime (submicrometer-thick electrochemical cell requirement). We conducted synchrotron operando liquid FY-XRM to track the nanoscale SOC of $LiFePO_4$ platelet and ellipsoidal particles in real time and with single particle sensitivity while the electrodes cycled. Our results show that the lithiation pathway differs substantially for platelet and ellipsoidal particles. In ellipsoidal particles, Li intercalates sequentially (particle-by-particle), forming a mosaic pattern of Li-rich and Li-poor particles. Here, the electrochemical current is concentrated in a small minority of actively (de)lithiating particles, consistent with previous studies.[4,5,13] In platelet particles, on the other hand, Li intercalates simultaneously in most particles, giving rise to a significantly more uniform current distribution and higher electrode utilization. We propose that the different intercalation pathways arise from differences in the surface reaction rate or the particle size, which are results of different synthesis conditions.

2. Results

2.1. Particle Synthesis and Morphology

Two carbon-coated $LiFePO_4$ particle morphologies were investigated: highly faceted commercial ellipsoidal particles[12] (Figure 1c) and low aspect ratio platelet particles synthesized using a solvothermal approach[45] (Figure 1d, see the Experimental Section for details). TEM of both particle morphologies show that the particles are single-crystalline-like without significant grain or domain boundaries (Figure S1, Supporting Information). The ellipsoidal particles are ≈230 nm in the major axis and ≈160 nm in the minor axis.[12] The average diffusion length along the [010] crystallographic axis, therefore, lies somewhere between the two values (divided by two). The platelet particles are ≈3 µm in length and width and ≈300 nm thick with large exposed (010) facets (Figure 1d), consistent with literature reports.[45–48] Even considering the uncertainty of the diffusion length in the ellipsoidal particle, the difference in the average diffusion length of the two particle morphologies is no greater than a factor of 2. The characteristic solid-state Li diffusion time is estimated to be <0.1 s.[46] Finally, these particles are sufficiently large such that the $LiFePO_4$ phase behavior is not significantly affected by the particle size,[17,49–52] as discussed later.

2.2. FY-XRM Platform

We designed and fabricated an operando electrochemical cell that houses a working electrode, organic liquid electrolyte ($LiClO_4$ salt dissolved in ethylene carbonate (EC) and dimethyl carbonate (DMC)), and a lithium foil counter electrode (Figure 1b). The ≈10 µm thick working electrode is a porous composite consisting of carbon-coated $LiFePO_4$, polyvinylidene fluoride (PVDF) and carbon black on a 50 nm thick Si_3N_4 membrane (Figure 1a, see the Experimental Section for details on cell assembly). Six consecutive galvanostatic charge and discharge cycles of the $LiFePO_4$ particles in the electrochemical cell at a rate of ≈0.2 C (where C indicates the rate at which it takes 1 h to charge or discharge the battery) yield the expected $LiFePO_4$ plateau voltage (Figure S2, Supporting Information).

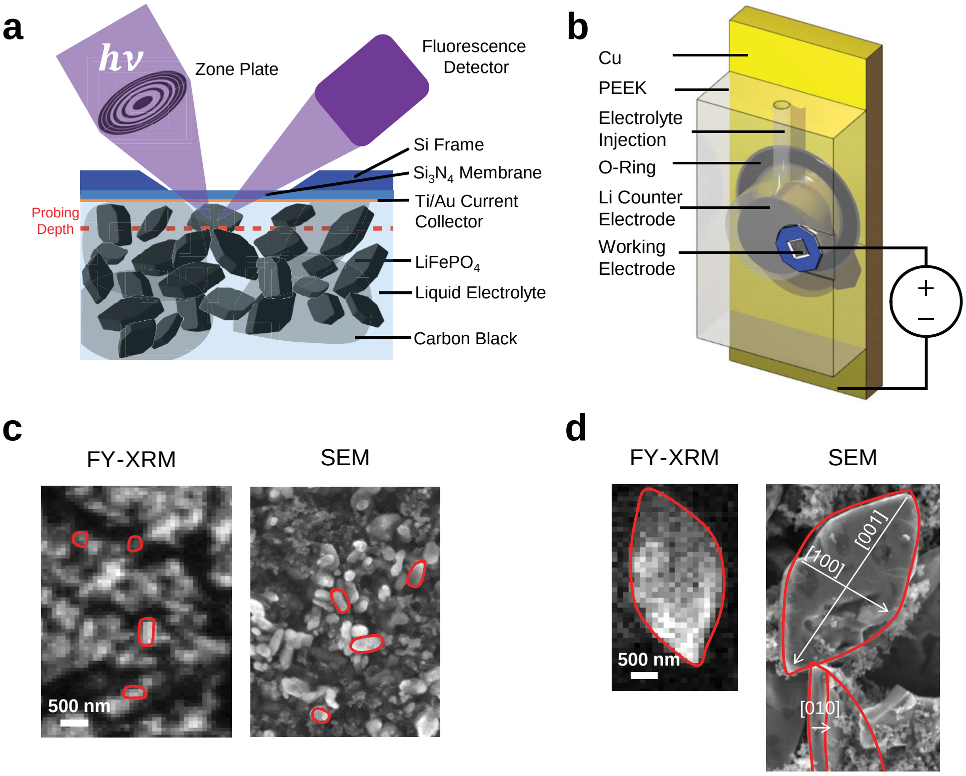

Figure 1. Liquid operando FY-XRM. a) A schematic of the ≈10 μm thick $LiFePO_4$ working electrode and the position of the X-ray beam and detector. Due to its shallow probing depth, FY-XRM is sensitive to individual nanoparticles inside an electrode. b) Schematic of the electrochemical cell used in FY-XRM, which contains a $LiFePO_4$ working electrode, a Li counter electrode, and organic liquid electrolyte in a PEEK housing. c) FY-XRM and SEM of representative ellipsoidal particles in a porous electrode. d) FY-XRM and SEM of platelet particles. FY-XRM is conducted with the electrode immersed in an organic liquid electrolyte, while SEM is conducted on dried samples. Bright pixels in FY-XRM show $LiFePO_4$ particles in the probing depth, whereas dark pixels indicate electrolyte, carbon, and/or binder. Representative particles are circled in red.

The coulombic efficiency is above 97%, and the electrochemical robustness of this cell is significantly improved over the microfluidic cells typically used in operando nanoparticle imaging experiments, which are cycled potentiostatically[29–32] or galvanostatically with low coulombic efficiency.[33]

We performed synchrotron FY-XRM on the $LiFePO_4$ electrodes housed inside this electrochemical cell at beam line 11.0.2 in the Advanced Light Source.[53,54] We raster-scanned a focused X-ray beam across the porous electrode, with a beam spot size of ≈75 nm, and measured the fluorescence-yield intensity at every pixel. The measurement time is 100 ms per pixel, currently limited by the fluorescence detector readout time. Imaging conditions were optimized to balance spatial and temporal resolutions, field of view, and sample stability under the beam. By changing the X-ray zone plate, which controls the beam spot size, the spatial resolution of FY-XRM can be improved to ≈25 nm, similar to that of standard scanning transmission X-ray microscopy.[13,53,54] Soft X-ray FY-XRM has previously been used to map arsenic in dried bacteria samples.[55] With a probing depth of a few hundred nm into the electrode,[56] FY-XRM images the single layer of particles closest to the thin-film current collector. Hence, particles in subsequent layers of the porous electrode do not convolute the acquired images. Figure 1c,d shows representative FY-XRM images and scanning electron micrographs (SEMs) of both particle morphologies.

To reveal an element's chemical state and electronic structure, we monitor the fluorescence-yield intensity as a function of the incident photon energy and use this signal to characterize the X-ray absorption spectrum. We determined the local lithium concentration in $LiFePO_4$ by quantifying the Fe oxidation state through nanoscale fluorescence-yield X-ray absorption spectroscopy (FY-XAS), which is a photon-in, photon-out spectroscopic technique.[57,58] **Figure** 2a–c shows typical single-pixel Fe L_3-edge absorption spectra for ellipsoidal particles. Fitting a linear combination of the reference spectra from electrochemically cycled $LiFe^{2+}PO_4$ and $Fe^{3+}PO_4$ samples to the single-pixel X-ray absorption spectrum[12,59] yields the nanoscale SOC.

We minimized the samples' exposure to X-rays by performing FY-XAS at carefully selected photon energies. Specifically, we collected the FY-XAS intensity for each pixel at 707 and 710 eV; these energies yield significant contrast between the discharged $LiFe^{2+}PO_4$ and charged $Fe^{3+}PO_4$ end-member phases. The two-energy linear combination analysis yielded SOCs essentially identical to the values obtained from the full-spectrum linear combination analysis (Figure 2d). As we will show later, the SOCs determined via FY-XRM closely match the SOCs measured electrochemically, confirming that the images taken within the probing depth are sufficiently representative of the electrodes' overall behavior.

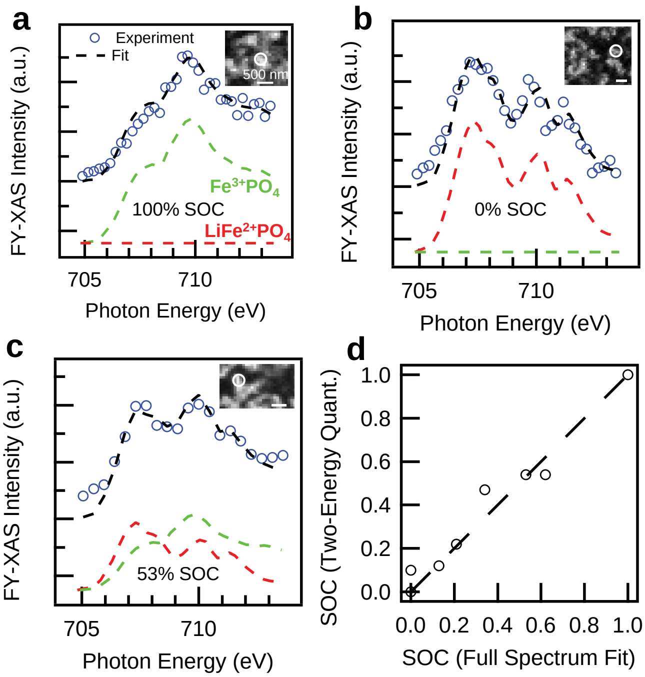

Figure 2. Nanoscale FY-XAS of LiFePO$_4$. a–c) Single-pixel FY-XAS at various SOCs, acquired by collecting the Fe fluorescence yield across the Fe L$_3$ absorption edge. A linear combination of the fully charged (Fe^{3+}PO$_4$) and fully discharged (LiFe^{2+}PO$_4$) reference spectra (broken red and green lines) was fitted to the experimental spectrum to calculate the single-pixel SOC. The insets contain the FY-XRM images of the region around the pixel (circled). d) Comparison of the SOCs calculated through a linear combination fit of the full spectrum to the two-energy quantification.

To optimize imaging conditions, we quantified sample stability under the X-ray beam using the nanoscale SOC as an indicator. **Figure 3** plots the frame-averaged SOC as a function of the X-ray dose, where the frame-averaged SOC is defined as the average SOC of every pixel weighed by the amount of Fe in the pixel. For platelet particles, the SOCs do not change even under the highest dose conditions examined (Figure S3a, Supporting Information). Therefore, we use a dose of 26 × 10^7 Gy per frame during operando imaging. For ellipsoidal particles, on the other hand, FY-XAS shows that sufficiently high X-ray doses can reduce Fe^{3+} to Fe^{2+} in the absence of electrochemical current (Figure S3b, Supporting Information). Specifically, the onset of beam-induced reduction occurs around a dose of 20 × 10^7 Gy (Figure 3). Therefore, we limited the maximum dose in our operando imaging of ellipsoidal particles to 8 × 10^7 Gy per frame. Imaging a fully charged cluster of ellipsoidal particles at this dose yields a frame-averaged SOC of ≈96%, showing negligible reduction of LiFePO$_4$.

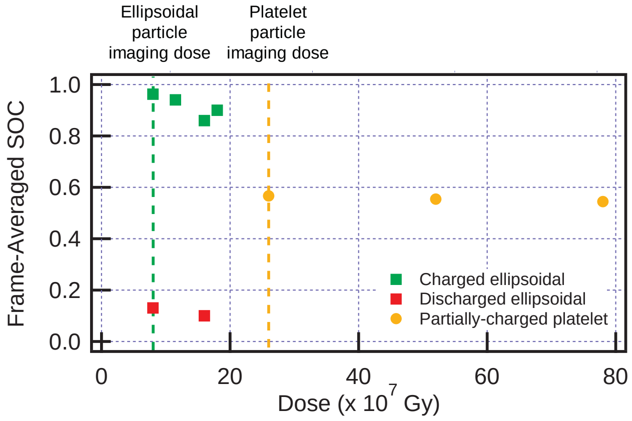

Figure 3. Sample stability under the X-ray beam. Increased X-ray dose lowers the SOC of a region by reducing Fe^{3+}PO$_4$ to LiFe^{2+}PO$_4$. The platelet particles show negligible reduction, whereas the ellipsoidal particles show slight reduction. X-ray imaging dosages were chosen within the stability window. Increased dose, or aggregate exposure to X-rays, is achieved by increased flux, decreased step size (increased spatial resolution), increased acquisition time, and/or repeatedly imaging the same region. The doses used for the SOC imaging experiments are indicated.

2.3. Operando SOC Mapping of Platelet Particles

We first demonstrate FY-XRM's ability to track the progression of lithiation within individual platelet particles. Operando FY-XRM was conducted on ten platelet particles which are oriented perpendicular to the X-ray beam while the electrode was discharged at a constant current of ≈0.2 C and ≈0.6 C. As a 2D imaging technique, FY-XRM averages the SOC along the platelet particles' [010] direction (**Figure 4**a–e). Due to the low aspect ratio of the platelet particles, SOC gradients in the fast-diffusion [010] direction are negligible.

First, we discuss the single-particle SOC, averaged per particle. Figure 4f shows the average SOC of each particle as a function of time. Specifically, for a half-discharged electrode, every particle observed is actively discharging, in which the SOC of every particle decreases significantly between imaging frames. This observation indicates that Li intercalates in these particles simultaneously. Here, the electrochemical current is homogeneously distributed to most particles in the electrode, despite variations in the particle size. This shows that the local current density of individual particles is approximately equal to the average current density of the electrode. This contrasts with our recent findings of particle-by-particle lithiation at comparable rates,[13] a point which we will return to later. We repeated this measurement for another batch of solvothermally synthesized platelet particles and also observed that all particles intercalate simultaneously.

Next, we turn to the nanoscale Li migration within individual particles. Our results show a complex pattern of Li-rich (red) and Li-poor (green) domains, and significant portions of each particle exhibit intermediate states of lithiation (yellow). In contrast, ex situ SOC images of LiFePO$_4$ platelet particles[14–16] show a single sharp, diamond-shaped phase boundary, which has been attributed to surface wetting and coherency strain.[17] The observed differences likely arise because ex situ microscopy captures the Li distribution within a particle after it has relaxed to its equilibrium state. A sharp phase boundary is energetically favorable because it minimizes the mixing penalty between lithiated and delithiated domains.[26,60]

When a particle is actively lithiating, as observed here, the domain boundaries would widen considerably if lithiation proceeds via a single-phase intercalation pathway.[26,60] In LiFePO$_4$, the intersections of the boundaries with the carbon coating

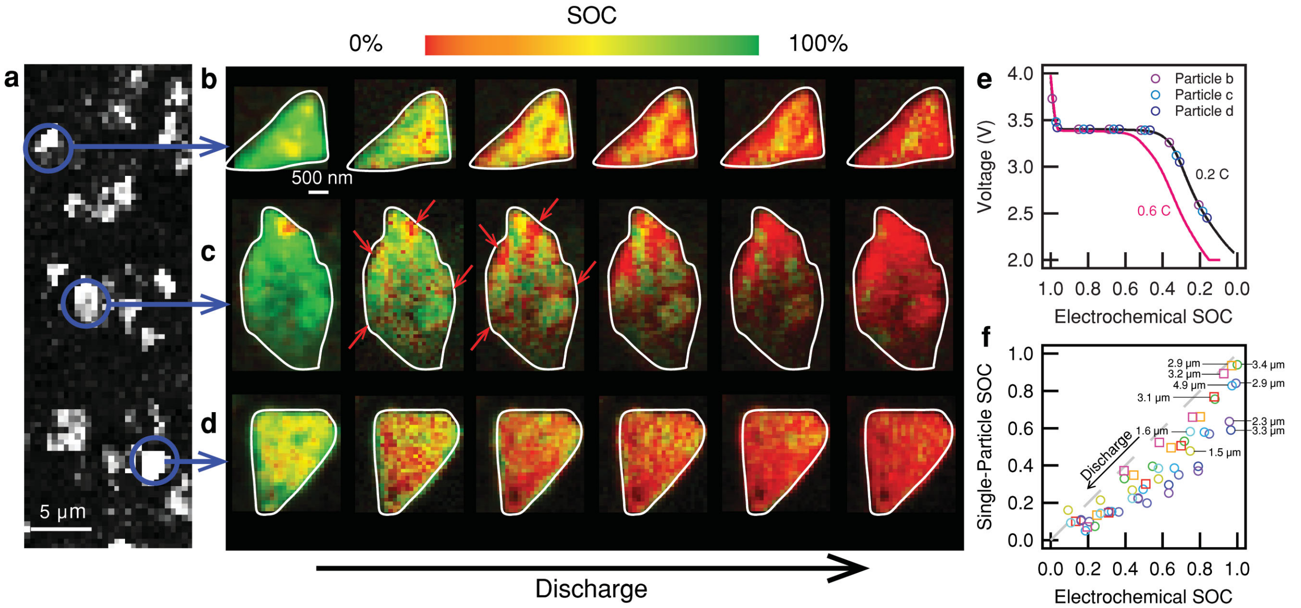

Figure 4. Operando SOC maps of platelet $LiFePO_4$ particles. a) FY-XRM image of the electrode taken at a single energy. b–d) SOC maps of three representative $LiFePO_4$ platelet particles as the electrode discharges at a rate of 0.2 C imaged with a 100 nm step size. The hue of each pixel represents the SOC and the brightness represents the amount of Fe within the probing depth. Red arrows in (c) point to electrochemical hotspots. The brightness difference along the vertical direction in (c) is explained by a slight tilt of the particle. e) The electrochemical profile of the electrode during discharge. The circles indicate the SOC of the electrode at the time each frame in (b–d) was imaged. f) The SOC of individual particles when the electrode discharged at 0.2 C (circles) and 0.6 C (squares). Each color represents one particle. The size of each particle, measured as the length of the longest dimension in the FY-XRM images, is indicated.

and the electrolyte form the active sites for Li insertion. Phase-field models have predicted sharp domain boundaries at very slow rates of cycling, considerably wider boundaries at higher cycling rates, and the disappearance of domain boundaries beyond a critical current.[26,60] Since lithiation is limited by the surface reaction,[61] domain boundaries widen and eventually disappear at higher cycling rates to accommodate more surface area for Li intercalation, thus decreasing the current density and reaction overpotential. Our experimental observations show that a ≈0.2 C rate is fast enough to significantly widen the domain boundary for platelet particles, and indirectly suggest a single-phase intercalation pathway, though the evidences here are far from definitive.[25,26,62] Additionally, the Li-rich/poor diamond-shaped cores observed ex situ[14–16] likely result from the interaction of coherency strain with Li wetting of certain crystal facets;[17] when cycled above a certain current, however, spatial variations in the exchange current density will reduce the effect of wetting and coherency strain. The absence of a diamond-shaped Li-rich/poor core and the presence of electrochemical hotspots (indicated by red arrows) are clearly visible in the particle depicted in Figure 4c, which has a similar size and shape as the particles used in ex situ images. Finally, we note that some of the hotspots may result from cracks or defects.

2.4. Operando SOC Mapping of Ellipsoidal Particles

To investigate how a different synthesis route affects the intercalation pathway, we tracked lithiation in highly faceted ellipsoidal particles synthesized through a solid-state process. With an average particle size of 230 nm, the diffusion length is similar to that of the platelet particles. We used FY-XRM to image 61 frames of 3 × 3.5 µm or 4 × 4.7 µm regions in the electrode as the battery cell was charged and discharged at a rate of C/3, C/2, and 1 C (Figure S4, Supporting Information). Each frame contains ≈100 $LiFePO_4$ primary particles within the probing depth, and isolated particles are visible in Figure 1c. In order to sample a large portion of the electrode to attain an accurate representation of the electrodes' ensemble behavior, we raster-scanned a different region of the electrode in each image. This approach also minimizes X-ray-induced damage.

Figure 5 shows the real-time SOC frames and the corresponding voltage curve recorded during discharge at a rate of 1 C. The SOC variation within each frame shows significant SOC heterogeneity in the porous electrode during cycling. During discharge, several Li-rich particles (red, circled) appear in frame (b), where the frame-averaged SOC is 89%. These are the first particles to lithiate. At a frame-averaged SOC of 44%, frame (e) reveals distinct clusters of Li-rich and Li-poor pixels. Finally, in frame (g), where the frame-averaged SOC is 18%, there are several Li-poor particles (green, circled), which are the last particles to lithiate. In contrast to the platelet particles, highly lithiated and delithiated ellipsoidal particles exist side-by-side across all cycling rates for both charge and discharge. These mosaic patterns indicate that most particles have either finished (de)lithiation or not yet started (de)lithiation, and validate the proposed particle-by-particle intercalation pathway based on ex situ microscopy.[4,5,12,13,27,28] Since the number of actively intercalating particles is small, the local current density for

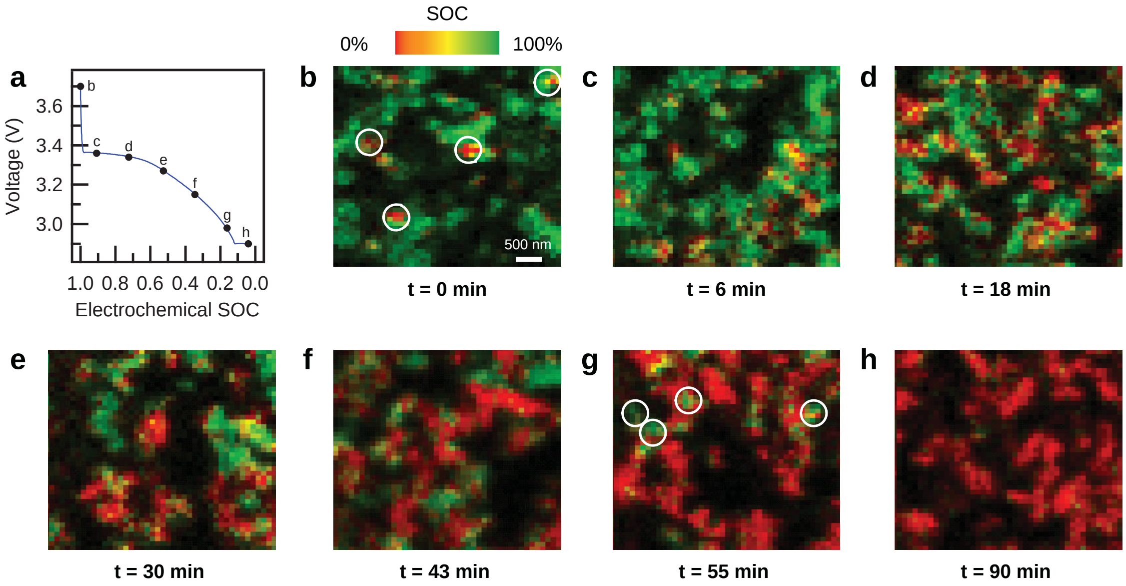

Figure 5. SOC maps of ellipsoidal $LiFePO_4$ during discharge at 1 C. a) The voltage profile of the electrochemical cell. b–h) SOC maps of the electrode imaged with a 90 nm step size. $t = 0$ min indicates the time when the discharge cycle starts. Frame (b) was taken before the discharge cycle while frame (h) was taken after the electrode was fully discharged. To minimize beam damage, each frame images a different region of the electrode.

active particles is at least an order of magnitude larger than the average current density of the electrode.[13]

Because the particles are closely packed in a technologically relevant fashion, it is difficult to directly assess the SOC of individual particles. Instead, we analyze the distribution of the single-pixel SOC values. Specifically, we evaluate the root mean square (RMS) of the difference between the single-pixel SOC and the corresponding frame-averaged SOC. Figure S5a (Supporting Information) plots the experimental RMS values as well as two bounding limits (see the Experimental Section for details). In the uniform limit, where all particles intercalate simultaneously (neglecting SOC variations within a single particle), the SOC of each pixel tracks the frame-averaged SOC, yielding a RMS value of 0. In the mosaic limit where particles intercalate sequentially, the RMS varies with the frame-averaged SOC and peaks at a value of 0.5. Figure S5b (Supporting Information) shows the SOC distribution of a simulated SOC map in the uniform and the mosaic limit. While the experimental SOC heterogeneity (Figure S5a, Supporting Information) lies between the two bounds, the RMS of the electrode better resembles the mosaic than the uniform limit. Some of the deviation from the mosaic limit may result from undersampling using a 75 nm wide beam. We note that our results differ from a recent TXM report showing simultaneous intercalation at low cycling rates for a similar $LiFePO_4$ morphology.[39] We attribute this difference to the sensitivity of soft X-rays to a single layer of particles in FY-XRM, whereas hard X-rays in TXM average the information for all particles along the path of the incident beam.

Finally, we show that the frame-averaged SOCs track the electrochemical SOCs, determined by integrating the current with regards to time for all cycling conditions (**Figure 6**). This agreement results from a large number of particles sampled in each frame and confirms each imaging frame is sufficiently representative of the porous electrode under the rates examined. This result also confirms the robustness of the electrochemical cell and the SOC quantification protocol.

3. Discussion

We have successfully tracked the nanoscale intercalation pathway of platelet and ellipsoidal $LiFePO_4$ particles during electrochemical cycling in an organic liquid electrolyte. Our results show a clear dichotomy in the intercalation pathway of the ellipsoidal and platelet particles (**Figure 7**). In platelet particles, lithiation proceeds concurrently in most particles, whereas in ellipsoidal particles, lithiation proceeds sequentially, with only a small fraction of particles intercalating at

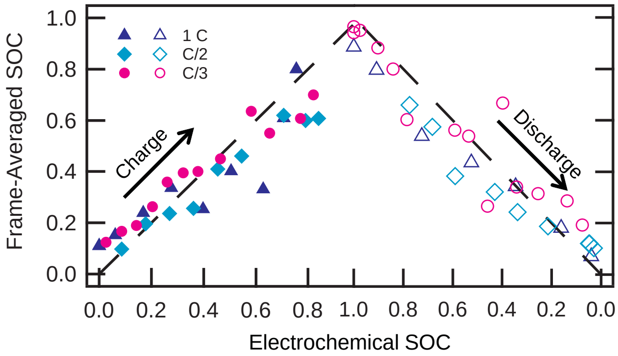

Figure 6. Comparison of the frame-averaged and electrochemical SOC. The frame-averaged SOC is determined by averaging the single-pixel SOC in each frame. The electrochemical SOC is determined by integrating the current with respect to time. The agreement with the expected 1:1 correlation (broken line) is excellent.

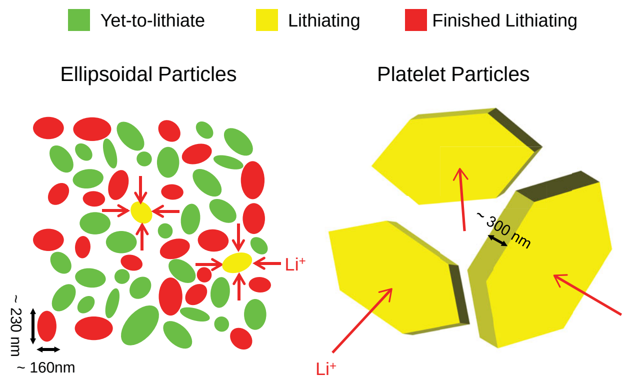

Figure 7. Schematic of the dichotomy in the intercalation pathway between the two types of particles. As revealed by FY-XRM, the ellipsoidal particles synthesized through solid-state methods lithiate sequentially, with only a small number of particles discharging at any one time. Conversely, the platelet particles synthesized solvothermally lithiate simultaneously. The immediate implication is that the electrochemical current (represented by the arrows) is far more concentrated in the ellipsoidal particles than in the platelet particles, by at least one order of magnitude. For simplicity, the distribution of Li within a particle is not shown.

any time. This dichotomy reflects the time needed to lithiate a single particle, which is given by product of the time needed to lithiate the entire electrode (e.g., discharging time) and the fraction of actively intercalating particles. Because the platelet particles intercalate concurrently (100% active particles), the time to lithiate a single particle nearly equals the time to lithiate the entire electrode: at a global cycling rate of 0.6 C, it would take ≈1.7 h to lithiate a single particle. On the other hand, the ellipsoidal particles intercalate sequentially: with less than 10% of the particles actively intercalating,[13] it takes less than 6 min for a single particle to lithiate at a global cycling rate of 1 C. Since the lithiation time is inversely related to the single-particle current density, our results suggest that the current density in ellipsoidal particles is at least an order of magnitude higher than that in platelet particles. We consider several plausible origins of the dichotomy in the intercalation pathway: differences in the miscibility gap, bulk diffusion, concentration of antisite defects, particle size, and surface reactivity.

We first consider the thermodynamics of the Li-rich and Li-poor phases of $LiFePO_4$ within the bulk of the particles. Figure S6 (Supporting Information) plots the voltage curves of the platelet and of the ellipsoidal particles at low cycling rates. Both particle morphologies exhibit the same voltage plateau at 3.42 V versus Li/Li^+, a similar voltage hysteresis of 50 mV at low rates of cycling, and essentially identical miscibility gap. These values are consistent with previous reports[5] and indicate that the thermodynamics of lithiation in both morphologies are comparable. This similarity in the thermodynamics is likely due to the relatively large dimensions of the particles: the phase diagram of $LiFePO_4$ has been shown to be largely independent on size for particles larger than 100 nm.[17,50]

Next, we consider the effect of crystallinity and particle size on diffusion in the solid. As previously discussed, both the platelet and ellipsoidal particles are mostly single crystalline (Figure S1, Supporting Information), and have a Li diffusion time <0.1 s,[46] a value which is significantly shorter than the charging and discharging time in these experiments. Due to the dissimilar synthesis conditions, the concentration of antisite defects, which block the 1D Li conduction channels,[63] may differ between the two morphologies. Assuming that the antisite defect concentration reach its equilibrium value during the platelet particles' 600 °C anneal, we estimate the concentration to be on the order of 0.1% with a defect formation energy of 0.55 eV.[63] At this concentration and given the dimension along the [010] crystallographic axis, very few diffusion channels will be blocked for a 300 nm thick particle.[63] As discussed by Amin, Maier et al.,[64–67] antisite defects (specifically $\left[\mathrm{Fe}_{\mathrm{Li}}^{\bullet}\right]$) and background impurities can serve as dopants in $Li_{1-x}FePO_4$. A minor variation in the dopant concentration will shift the boundary of the charge-compensation regimes between $\left[V'_{\mathrm{Li}}\right]=\left[\mathrm{Fe}_{\mathrm{Li}}^{\bullet}\right]$ and $\left[V'_{\mathrm{Li}}\right]=\left[h^{\bullet}\right]$, and therefore impact the dependence of electrical conductivity on the lithium activity. Nevertheless, we note that the lithium vacancy concentration at the edge of the miscibility gap is likely on the order of a few percent, and probably greater than the antisite defect and impurity concentration. Moreover, given the small diffusion lengths, dramatic change in the defect concentrations and mobilities are needed to alter the Li intercalation from being surface reaction limited to bulk diffusion limited.

Based on the arguments presented above, the observed dichotomy in the active particle fraction is not likely attributed to bulk thermodynamic or diffusion properties. If we assume that lithiation proceeds via a single-phase, solid solution intercalation pathway, which is supported by increased theoretical[25,26,60] and experimental[24,34] evidence, then the lithiation time of a single particle is determined by the exchange current density and the particle thickness[13] (under the assumption that Li inserts into a particle on the surface parallel to the fast [010] diffusion axis). Because the particle thickness only varies by a factor of ≈2 between the platelet and the ellipsoidal particles, we propose that the exchange current density of the two particle morphologies are significantly different, giving rise to dissimilar local current densities, consistent with a surface-limited reaction.[61] Phase-field porous-electrode simulations have also showed that lowering the exchange current density result in more concurrent intercalation.[13] The difference in exchange current density likely arises from the different synthesis conditions. The reduced exchange current density results in increased single-particle lithiation time and the observed concurrent intercalation in platelet particles. One possible origin is that the smoother $LiFePO_4$ platelet particles have a lower surface reactivity than the highly faceted ellipsoidal particles. Lending support to this hypothesis, it was recently shown that wet-etching platelet particles introduces rougher facets and improves the surface kinetics.[68] Point and extended defects on the surface may also result in differences in the exchange current density. For instance, possible variations in the antisite defect concentration could contribute to differences in the exchange current densities.

We also consider the possibility that $LiFePO_4$ lithiates via a nucleation and growth pathway,[4,69,70] though experimentally we do not observe sharp phase boundaries. In contrast to the solid-solution pathway, the larger size of the platelet particles results in the increased lithiation time. In this pathway, at least one nucleation event is necessary to initiate lithiation per particle, and the lithiation front cannot propagate beyond the boundary of the particle.[71,72] In this limit of a single nucleation event per particle, like in the domino cascade model,[4] the lithiation time is proportional to the length of the particle along the growth direction.[69] The platelet particles (≈3 µm) are over an order of magnitude longer than the ellipsoidal particles (≈200 nm), and may explain why it takes more time to lithiate a platelet particle. Given the relatively large size of the platelet particles, however, it is conceivable that each particle undergoes more than one nucleation event. As a result, the multiple lithiation fronts per particle can shorten the time needed to lithiate a single particle, which is expected to lower the difference in the lithiation time between the platelet and ellipsoidal particles. We note that the rate of nucleation and the wave propagation velocity may differ between the two morphologies as a result of the different synthesis procedures. Bulk, surface or topological defects may also affect the rate of nucleation and growth. At this point, X-ray microscopy cannot definitively distinguish the solid solution from the nucleation and growth pathway. We anticipate that additional research would elucidate this point.

Understanding the influence of the synthesis on the lithiation pathway provides guidance toward improving the design of nanostructured particles for Li-ion batteries. By varying the synthesis conditions, it is possible to vary the fundamental intercalation behavior as well as the performance of the battery. Our work shows that the ellipsoidal particles synthesized through solid-state methods lithiate faster. For solvothermally synthesized platelet particles, however, the current is more uniformly distributed, and the more homogeneous electrode may result in increased cycle life and durability.[13,73] These guidelines can be used to synthesize and engineer particles to match performance requirements.

4. Conclusions

In summary, we developed an operando fluorescence-yield X-ray microscopy platform to track the local SOC of $LiFePO_4$ porous electrodes in an organic liquid electrolyte with single particle sensitivity. Using operando liquid FY-XRM, we demonstrate unambiguously that ellipsoidal particles intercalate sequentially, whereas platelet particles intercalate concurrently. The local current density, a key parameter that influences electrode degradation, differs by at least one order of magnitude between the two particle morphology for comparable electrode cycling rates. Thus, the synthesis conditions of battery particles directly alter the intercalation pathway. Our work shows that FY-XRM is a promising technique to elucidate and quantify many heterogeneous nanoscale processes within liquid environments.

5. Experimental Section

Synthesis of $LiFePO_4$ Platelet Particles: Synthesis was conducted using a solvothermal method with a mixed water and polyethylene glycol solvent[45] in an N_2 environment. 6 mL of 1 M $H_3PO_{4(aq)}$ (Sigma-Aldrich 345325) was mixed with 18 mL of polyethylene glycol 400 (Sigma-Aldrich 202398). 18 mL of 1 M $LiOH{\cdot}H_2O_{(aq)}$ (Sigma-Aldrich 62528) was added to the mixture to create the creamy-white precipitate Li_3PO_4. Afterward, 12 mL of 0.5 M $FeSO_4{\cdot}7H_2O_{(aq)}$ (Sigma-Aldrich F7002) was added to the precipitate and stirred for ≈10 min. The suspension was transferred to a Teflon-lined autoclave and heated at 140 °C for 24 h. The $LiFePO_4$ precipitate was washed and centrifuged three times with deionized water and dried under vacuum at ≈50 °C. Powder diffraction shows that the synthesized $LiFePO_4$ is pure-phase (Figure S7, Supporting Information). To carbon-coat the $LiFePO_4$ particles, the synthesized particles were mixed with sucrose (Sigma-Aldrich S5016) at a ratio of 5:1 $LiFePO_4$:sucrose by mass. The mixture was heated at 600 °C for 5 h under flowing Ar to complete carbon coating and improve $LiFePO_4$ crystallinity.[9] To measure the capacity of the particles, an electrode sheet consisting 74 wt% carbon-coated $LiFePO_4$, 20 wt% carbon black (Timcal C65), and 6 wt% PVDF (MTI Corporation) binder was mixed with *N*-methyl-2-pyrrolidone (NMP), cast on carbon-coated Al foil with a nominal thickness of 20 µm, and dried at 60 °C under atmosphere and subsequently at $t = 80$ °C under vacuum. Coin cells (size CR2016) containing a ≈9 mm $LiFePO_4$ electrode, two Celgard separators, a Li metal anode, and a 1 M $LiPF_6$ in 4:3:3 (wt/wt/wt) EC: diethyl carbonate: DMC electrolyte were assembled. The specific capacity was 150 mAh g^{-1} when cycled at C/60 (Figure S6a, Supporting Information). The ellipsoidal particles electrode used for electrochemical cycling characterization was prepared identically, except using commercial carbon-coated $LiFePO_4$ particles from Mitsui Engineering and Shipbuilding. The specific capacity was 160 mAh g^{-1} when cycled at C/30 (Figure S6b, Supporting Information).

Operando Electrochemical Cell: The electrochemical cell for FY-XRM consists of a working electrode, an inert polyether ether ketone (PEEK) housing, and a copper back plate (Figure 1b). A 5 nm Ti adhesion layer and a 4 nm Au current collector were evaporated on a 50 nm thick X-ray-transparent Si_3N_4 membrane (Figure 1a). To fabricate the ellipsoidal $LiFePO_4$ electrode, a slurry of 80 wt% carbon-coated $LiFePO_4$ (Mitsui Engineering and Shipbuilding), 15 wt% Timcal C65 carbon black, and 5 wt% PVDF in NMP was drop-cast on the Si_3N_4 stack and dried at ≈50 °C. The platelet $LiFePO_4$ electrode was fabricated identically, except using a slurry of 70 wt% carbon black, 25 wt% carbon-coated $LiFePO_4$, and 5% PVDF. The slurry was drop-cast on the current collector to create the $LiFePO_4$ electrode. The working electrode stack was assembled on the PEEK housing. Graphite conductive adhesive (Electron Microscopy Sciences 112) was used to adhere the Si_3N_4 membrane and the working electrode to the PEEK housing and provide external electronic contact. After the adhesive dried, Torr Seal (Varian) was applied to complete the seal between the Si_3N_4 membrane and the PEEK housing. Cell assembly was completed in an Ar-filled glovebox. For the counter-electrode, a Li foil ≈7 cm in diameter was pressed onto an elevated platform on the copper back plate. The PEEK and copper companion pieces were sealed using screws and a fluoropolymer O-ring (Kalrez 4375 UP). An electrolyte consisting of 1.0 M $LiClO_4$ salt in a 1:1 (wt/wt) EC:DMC solution was injected into the assembled cell. The electrolyte injection hole was sealed using the electrolyte-compatible epoxy Hardman 4001.[74] The distance between the working electrode and counter electrode is ≈300 µm, which is sufficiently small to prevent bulk electrolyte diffusion limitations under the current densities employed in the experiment. After assembly, the sealed cell was removed from the glovebox and cycled in air. The ellipsoidal particle cell was cycled six times at a constant current of 1 µA between 3.7 and 2.9 V. The capacity was ≈7.5 µAh. The platelet particle cell was cycled at a constant current of 0.25 µA between 3.7 and 2.5 V with an initial capacity of ≈0.9 µAh that rises to ≈1.5 µAh after ten cycles. Typical formation cycles are given in Figure S2 (Supporting Information). All electrochemical cycling was done using a BioLogic VSP-300 potentiostat.

Reference Spectra for Ellipsoidal Particles: We acquired the reference spectra (Figure 2a–c) used for SOC mapping of ellipsoidal particles from fully charged and fully discharged electrodes. The electrodes containing ellipsoidal particles were prepared in coin cells, which underwent five formation cycles between 3.8 and 2.5 V at a rate of C/10 for charging and C/5 for discharging. Subsequently, the fully charged $Fe^{3+}PO_4$ reference underwent a C/15 charge cycle to 3.8 V, while the fully discharged $LiFe^{2+}PO_4$ reference was kept in a discharged state. The cells were disassembled in an Ar glovebox, rinsed with excess dimethyl carbonate, and dried. Reference absorption spectra were taken from the dried electrodes using FY-XRM. To normalize the spectra consistently with past $LiFePO_4$ X-ray spectro-microscopy reports,[12,13] the fluorescence yield at 705 eV is set to 0 and the fluorescence yield at the white line (energy of highest absorption and fluorescence) is set to 1. Previous SOC measurements of the same particles cycled to the same voltage show that the particles are indeed fully charged and fully discharged.[12]

FY-XRM Imaging Geometry: FY-XRM was conducted using the scanning transmission X-ray microscope at beam line 11.0.2 at the Advanced Light Source in Lawrence Berkeley National Laboratory.[53] A 60 nm zone plate focuses the incident X-ray to a ≈75 nm spot size, while an interferometer-controlled stage raster-scans the position of the electrochemical cell.[75] The electrochemical cell is tilted 30° with respect to the normal of the X-ray beam (Figure 1a). The fluorescence X-rays at energies between 660 and 750 eV are collected using an Amptek X123-SDD X-ray detector. When imaging ellipsoidal particles, we control the incident X-ray flux to be $\approx 3 \times 10^7$ photons per second by using a 10 µm dispersive slit and a 10 µm nondispersive slit. The dose was $\approx 4 \times 10^7$ Gy per photon energy during imaging, or 8×10^7 Gy per frame. The platelet SOC maps were obtained at a dose of $\approx 26 \times 10^7$ Gy per frame using 20 µm slits. To change the dose for the beam damage experiments in Figure 3, we increased the size of the slits to increase the flux, decreased the step size, increased the exposure time, and/or repeatedly imaged the same region.

Two-Energy X-Ray Absorption Quantification: The FY-XAS was used to quantify the SOC at every pixel. We acquired the fluorescence yield intensity at two photon energies, 707 and 710 eV. We solved for the $LiFe^{2+}PO_4$ phase (a) and $Fe^{3+}PO_4$ phase (b) in each pixel:

$$\begin{bmatrix} S_{707} \\ S_{710} \end{bmatrix} = \begin{bmatrix} \mathrm{LFP}_{707} & \mathrm{FP}_{707} \\ \mathrm{LFP}_{710} & \mathrm{FP}_{710} \end{bmatrix} \begin{bmatrix} a \\ b \end{bmatrix} \tag{1}$$

where S_{707} and S_{710} represent the single-pixel Fe FY-XAS intensity taken at 707 and 710 eV. For the ellipsoidal particles, LFP_{707}, LFP_{710}, FP_{707}, and FP_{710} references were taken through a cubic spline interpretation of the fluorescence yield at 707 and 710 eV of the fully discharged ($LiFe^{2+}PO_4$) and fully charged ($Fe^{3+}PO_4$) reference samples. The SOC is given by $\mathrm{SOC} = b/(a+b)$. The brightness is given by the sum $a + b$, representing the total iron content in the pixel. If either a or b is less than 0, then it is set to 0. For the platelet particles, the references for the FP_{707} and FP_{710} spectra were taken by performing in situ FY-XRM for a fully charged particle where the electrode voltage was held at 4 V. The LFP_{707} and LFP_{710} references were taken from the same particle discharged to 2 V. To ensure that the particle was fully discharged, we compared its FY-XAS to a different particle that was previously not exposed to X-rays and found very similar results. We performed the SOC quantification on the reference particle and showed that it is indeed uniformly charged and discharged (Figure S8, Supporting Information).

Frame-Averaged SOC: To calculate the frame-averaged SOC ($\overline{\mathrm{SOC}}$), we apply the following formula:

$$\overline{\mathrm{SOC}} = \sum_i \frac{b_i}{a_i + b_i} \tag{2}$$

where a_i and b_i is the $LiFe^{2+}PO_4$ and $Fe^{3+}PO_4$ phase fraction at the ith pixel. The single-particle SOCs for the platelet particles were also calculated according to Equation (2). Here, a frame would only contain a single particle.

RMS Analysis: We apply the following formula to calculate the RMS of a single frame:

$$\mathrm{RMS} = \sqrt{\frac{1}{N-1} \sum_i^N \left(\mathrm{SOC}_i - \overline{\mathrm{SOC}}\right)^2} \tag{3}$$

where SOC_i is the SOC for the ith pixel, $\overline{\mathrm{SOC}}$ is the frame-averaged SOC, and N is the total number of bright pixels in the image. The confidence interval, plotted as error bars, for the RMS is given by

$$\sqrt{\frac{(N-1)\mathrm{RMS}^2}{\chi\left(\frac{a}{2}, N-1\right)}} \le \mathrm{RMS} \le \sqrt{\frac{(N-1)\mathrm{RMS}^2}{\chi\left(1-\frac{a}{2}, N-1\right)}} \tag{4}$$

where χ is the critical value for the Chi-squared distribution and a is chosen as 0.003 for a 99.7% confidence interval.

Uniform and Mosaic Limits: We simulated the RMS of a completely uniform and completely mosaic electrode. The uniform limit assumes the SOC of every pixel equals the frame-averaged SOC; as a result, the RMS for the uniform limit is always 0. The mosaic limit assumes the SOC of every pixel is either 0% or 100%. To visualize the limits in Figure S5b (Supporting Information), we altered the SOC of each pixel in Figure 5f in accordance to the uniform and mosaic limits. The brightness of a pixel indicates the amount of $LiFePO_4$ present and is proportional to the FY-XAS intensity. The brightest pixel in an imaging frame typically corresponds to a brightness of 100 counts. A pixel with low brightness indicates that there is no $LiFePO_4$ particle within the probing depth. In the root mean square analyses, pixels with brightness levels less than 20 counts are neglected due to low signal-to-noise.

Supporting Information

Supporting Information is available from the Wiley Online Library or from the author.

Acknowledgements

The research at Stanford was supported by Samsung Advanced Institute of Technology Global Research Outreach program, and startup funding from Stanford School of Engineering and the Precourt Institute for Energy. The Advanced Light Source was supported by the Director, Office of Science, Office of Basic Energy Sciences, of the U.S. Department of Energy under Contract No. DE-AC02-05CH11231. Y.L. was supported by the National Science Foundation Graduate Research Fellowship under Grant No. DGE-114747. The authors thank Mitsui Engineering and Shipbuilding for providing the ellipsoidal $LiFePO_4$ particles. Part of this work was performed at the Stanford Nano Shared Facilities (SNSF) at Stanford University. Finally, the authors are grateful to L. Zhang, S. Meyer, and A. C. Baclig at Stanford for helpful discussions and assistance with sample preparation.

Received: January 23, 2015
Revised: April 3, 2015

---

[1] A. K. Padhi, K. S. Nanjundaswamy, J. B. Goodenough, *J. Electrochem. Soc.* **1997**, *144*, 1188.

[2] M. Tang, W. C. Carter, Y.-M. Chiang, *Annu. Rev. Mater. Res.* **2010**, *40*, 501.

[3] R. Malik, A. Abdellahi, G. Ceder, *J. Electrochem. Soc.* **2013**, *160*, A3179.

[4] C. Delmas, M. Maccario, L. Croguennec, F. Le Cras, F. Weill, *Nat. Mater.* **2008**, *7*, 665.

[5] W. Dreyer, J. Jamnik, C. Guhlke, R. Huth, J. Moskon, M. Gaberscek, *Nat. Mater.* **2010**, *9*, 448.

[6] M. Gaberscek, R. Dominko, J. Jamnik, *Electrochem. Commun.* **2007**, *9*, 2778.
[7] J. Chen, M. Whittingham, *Electrochem. Commun.* **2006**, *8*, 855.
[8] C. A. J. Fisher, M. S. Islam, *J. Mater. Chem.* **2008**, *18*, 1209.
[9] M. S. Whittingham, *Chem. Rev.* **2014**, *114*, 11414.
[10] D. Larcher, J.-M. Tarascon, *Nat. Chem.* **2014**, *7*, 19.
[11] L. Wang, X. He, W. Sun, J. Wang, Y. Li, S. Fan, *Nano Lett.* **2012**, *12*, 5632.
[12] W. C. Chueh, F. El Gabaly, J. D. Sugar, N. C. Bartelt, A. H. McDaniel, K. R. Fenton, K. R. Zavadil, T. Tyliszczak, W. Lai, K. F. McCarty, *Nano Lett.* **2013**, *13*, 866.
[13] Y. Li, F. El Gabaly, T. R. Ferguson, R. B. Smith, N. C. Bartelt, J. D. Sugar, K. R. Fenton, D. A. Cogswell, A. L. D. Kilcoyne, T. Tyliszczak, M. Z. Bazant, W. C. Chueh, *Nat. Mater.* **2014**, *13*, 1149.
[14] U. Boesenberg, F. Meirer, Y. Liu, A. K. Shukla, R. Dell'anna, T. Tyliszczak, G. Chen, J. C. Andrews, T. J. Richardson, R. Kostecki, J. Cabana, *Chem. Mater.* **2013**, *25*, 1664.
[15] D. A. Shapiro, Y.-S. Yu, T. Tyliszczak, J. Cabana, R. Celestre, W. Chao, K. Kaznatcheev, A. L. D. Kilcoyne, F. Maia, S. Marchesini, Y. S. Meng, T. Warwick, L. L. Yang, H. A. Padmore, *Nat. Photonics* **2014**, *8*, 765.
[16] I. T. Lucas, A. S. Mcleod, J. S. Syzdek, D. S. Middlemiss, C. P. Grey, D. N. Basov, R. Kostecki, *Nano Lett.* **2015**, *15*, 1.
[17] D. A. Cogswell, M. Z. Bazant, *Nano Lett.* **2013**, *13*, 3036.
[18] S. Ferrari, R. L. Lavall, D. Capsoni, E. Quartarone, A. Magistris, P. Mustarelli, P. Canton, *J. Phys. Chem. C* **2010**, *114*, 12598.
[19] B.-J. Hwang, K.-F. Hsu, S.-K. Hu, M.-Y. Cheng, T.-C. Chou, S.-Y. Tsay, R. Santhanam, *J. Power Sources* **2009**, *194*, 515.
[20] S.-P. Badi, M. Wagemaker, B. L. Ellis, D. P. Singh, W. J. H. Borghols, W. H. Kan, D. H. Ryan, F. M. Mulder, L. F. Nazar, *J. Mater. Chem.* **2011**, *21*, 10085.
[21] Y. Wang, J. Wang, J. Yang, Y. Nuli, *Adv. Funct. Mater.* **2006**, *16*, 2135.
[22] Y. Orikasa, T. Maeda, Y. Koyama, H. Murayama, K. Fukuda, H. Tanida, H. Arai, E. Matsubara, Y. Uchimoto, Z. Ogumi, *J. Am. Chem. Soc.* **2013**, *135*, 5497.
[23] X. Zhang, M. van Hulzen, D. P. Singh, A. Brownrigg, J. P. Wright, N. H. van Dijk, M. Wagemaker, *Nano Lett.* **2014**, *14*, 2279.
[24] H. Liu, F. C. Strobridge, O. J. Borkiewicz, K. M. Wiaderek, K. W. Chapman, P. J. Chupas, C. P. Grey, *Science* **2014**, *344*, 1252817.
[25] R. Malik, F. Zhou, G. Ceder, *Nat. Mater.* **2011**, *10*, 587.
[26] P. Bai, D. A. Cogswell, M. Z. Bazant, *Nano Lett.* **2011**, *11*, 4890.
[27] G. Brunetti, D. Robert, J. L. Rouvi, E. F. Rauch, J. F. Martin, J. F. Colin, *Chem. Mater.* **2011**, *23*, 4515.
[28] D. Robert, T. Douillard, A. Boulineau, G. Brunetti, P. Nowakowski, D. Venet, P. Bayle-guillemaud, C. Cayron, *ACS Nano* **2013**, *7*, 10087.
[29] J. Y. Huang, L. Zhong, C. M. Wang, J. P. Sullivan, W. Xu, L. Q. Zhang, S. X. Mao, N. S. Hudak, X. H. Liu, A. Subramanian, H. Fan, L. Qi, A. Kushima, J. Li, *Science* **2010**, *330*, 1515.
[30] X. H. Liu, J. W. Wang, S. Huang, F. Fan, X. Huang, Y. Liu, S. Krylyuk, J. Yoo, S. A. Dayeh, A V Davydov, S. X. Mao, S. T. Picraux, S. Zhang, J. Li, T. Zhu, J. Y. Huang, *Nat. Nanotech.* **2012**, *7*, 749.
[31] F. Wang, H.-C. Yu, M.-H. Chen, L. Wu, N. Pereira, K. Thornton, A. Van der Ven, Y. Zhu, G. G. Amatucci, J. Graetz, *Nat. Commun.* **2012**, *3*, 1201.
[32] M. Gu, L. R. Parent, B. L. Mehdi, R. R. Unocic, M. T. McDowell, R. L. Sacci, W. Xu, J. G. Connell, P. Xu, P. Abellan, X. Chen, Y. Zhang, D. E. Perea, J. E. Evans, L. J. Lauhon, J.-G. Zhang, J. Liu, N. D. Browning, Y. Cui, I. Arslan, C.-M. Wang, *Nano Lett.* **2013**, *13*, 6106.
[33] M. E. Holtz, Y. Yu, D. Gunceler, J. Gao, R. Sundararaman, K. A. Schwarz, T. A. Arias, H. D. Abruña, D. A. Muller, *Nano Lett.* **2014**, *14*, 1453.
[34] J. Niu, A. Kushima, X. Qian, L. Qi, K. Xiang, Y.-M. Chiang, J. Li, *Nano Lett.* **2014**, *14*, 4005.
[35] J. Nelson, S. Misra, Y. Yang, A. Jackson, Y. Liu, H. Wang, H. Dai, J. C. Andrews, Y. Cui, M. F. Toney, *J. Am. Chem. Soc.* **2012**, *134*, 6337.
[36] J. Wang, Y. K. Chen-Wiegart, J. Wang, *Chem. Commun.* **2013**, *49*, 6480.
[37] M. Ebner, F. Marone, M. Stampanoni, V. Wood, *Science* **2013**, *342*, 716.
[38] J. N. Weker, N. Liu, S. Misra, J. C. Andrews, Y. Cui, M. F. Toney, *Energy Environ. Sci.* **2014**, *7*, 2771.
[39] J. Wang, Y. K. Chen-Wiegart, J. Wang, *Nat. Commun.* **2014**, *5*, 4570.
[40] A. Ulvestad, A. Singer, H.-M. Cho, J. N. Clark, R. Harder, J. Maser, Y. S. Meng, O. G. Shpyrko, *Nano Lett.* **2014**, *14*, 5123.
[41] J. Wang, Y. K. Chen-Wiegart, J. Wang, *Angew. Chem.* **2014**, *126*, 4549.
[42] Y.-S. Yu, C. Kim, Y. Liu, A. van der Ven, Y. S. Meng, R. Kostecki, J. Cabana, *Adv. Energy Mater.* **2015,** *5*, 1402040.
[43] B. L. Henke, E. M. Gullikson, J. C. Davis, *At. Data Nucl. Data Tables* **1993**, *54*, 181.
[44] E. M. Gullikson, X-Ray Interactions with Matter, http://henke.lbl.gov/optical_constants/ (accessed: Nov 2014).
[45] S. Yang, X. Zhou, J. Zhang, Z. Liu, *J. Mater. Chem.* **2010**, *20*, 8086.
[46] D. Morgan, A. Van der Ven, G. Ceder, *Electrochem. Solid-State Lett.* **2004**, *7*, A30.
[47] G. Chen, X. Song, T. J. Richardson, *Electrochem. Solid-State Lett.* **2006**, *9*, A295.
[48] M. E. Schuster, D. Teschner, J. Popovic, N. Ohmer, F. Girgsdies, J. Tornow, M. G. Willinger, D. Samuelis, M. Titirici, J. Maier, R. Schlo, *Chem. Mater.* **2014**, *26*, 1040.
[49] M. Tang, N. Meethong, W. C. Carter, *Chem. Mater.* **2009**, *21*, 1557.
[50] M. Wagemaker, D. P. Singh, W. J. H. Borghols, U. Lafont, L. Haverkate, V. K. Peterson, F. M. Mulder, *J. Am. Chem. Soc.* **2011**, *133*, 10222.
[51] M. Wagemaker, F. M. Mulder, A. Van der Ven, *Adv. Mater.* **2009**, *21*, 2703.
[52] G. Kobayashi, S. Nishimura, M.-S. Park, R. Kanno, M. Yashima, T. Ida, A. Yamada, *Adv. Funct. Mater.* **2009**, *19*, 395.
[53] H. Bluhm, K. Andersson, T. Araki, K. Benzerara, G. E. Brown, J. J. Dynes, S. Ghosal, M. K. Gilles, H.-C. Hansen, J. C. Hemminger, a. P. Hitchcock, G. Ketteler, A. L. D. Kilcoyne, E. Kneedler, J. R. Lawrence, G. G. Leppard, J. Majzlam, B. S. Mun, S. C. B. Myneni, a. Nilsson, H. Ogasawara, D. F. Ogletree, K. Pecher, M. Salmeron, D. K. Shuh, B. Tonner, T. Tyliszczak, T. Warwick, T. H. Yoon, *J. Electron Spectrosc. Relat. Phenom.* **2006**, *150*, 86.
[54] E. de Smit, I. Swart, J. F. Creemer, G. H. Hoveling, M. K. Gilles, T. Tyliszczak, P. J. Kooyman, H. W. Zandbergen, C. Morin, B. M. Weckhuysen, F. M. F. de Groot, *Nature* **2008**, *456*, 222.
[55] A. P. Hitchcock, M. Obst, J. Wang, Y. S. Lu, T. Tyliszczak, *Environ. Sci. Technol.* **2012**, *46*, 2821.
[56] X. Liu, D. Wang, G. Liu, V. Srinivasan, Z. Liu, Z. Hussain, W. Yang, *Nat. Commun.* **2013**, *4*, 2568.
[57] T.-K. Sham, *Adv. Mater.* **2014**, *26*, 7896.
[58] X. Liu, W. Yang, Z. Liu, *Adv. Mater.* **2014**, *26*, 7710.
[59] X. Liu, J. Liu, R. Qiao, Y. Yu, H. Li, L. Suo, Y. Hu, Y.-D. Chuang, G. Shu, F. Chou, T.-C. Weng, D. Nordlund, D. Sokaras, Y. J. Wang, H. Lin, B. Barbiellini, A. Bansil, S. Xiangyun, Z. Liu, S. Yan, G. Liu, S. Qian, T. J. Richardson, D. Pendergast, H. Zahid, F. M. F. de Groot, W. Yang, *J. Am. Chem. Soc.* **2012**, *134*, 13708.
[60] D. A. Cogswell, M. Z. Bazant, *ACS Nano* **2012**, *6*, 2215.
[61] M. Z. Bazant, *Acc. Chem. Res.* **2013**, *46*, 1144.
[62] H. Liu, F. C. Strobridge, O. J. Borkiewicz, K. M. Wiaderek, K. W. Chapman, P. J. Chupas, C. P. Grey, *Science* **2014**, *344*, 1252817.
[63] R. Malik, D. Burch, M. Bazant, G. Ceder, *Nano Lett.* **2010**, *10*, 4123.
[64] R. Amin, C. Lin, J. Maier, *Phys. Chem. Chem. Phys.* **2008**, *10*, 3524.
[65] J. Maier, R. Amin, *J. Electrochem. Soc.* **2008**, *155*, A339.
[66] C. Zhu, K. Weichert, J. Maier, *Adv. Funct. Mater.* **2011**, *21*, 1917.

[67] R. Amin, J. Maier, *Solid State Ionics* **2008**, *178*, 1831.
[68] A. Paolella, G. Bertoni, S. Marras, E. Dilena, M. Colombo, M. Prato, A. Riedinger, M. Povia, A. Ansaldo, K. Zaghib, L. Manna, C. George, *Nano Lett.* **2014**, *14*, 6828.
[69] G. K. Singh, G. Ceder, M. Z. Bazant, *Electrochim. Acta* **2008**, *53*, 7599.
[70] G. Oyama, Y. Yamada, R. Natsui, S. Nishimura, A. Yamada, *J. Phys. Chem. C* **2012**, *116*, 7306.
[71] P. Bai, G. Tian, *Electrochim. Acta* **2013**, *89*, 644.
[72] P. Bai, M. Z. Bazant, *Nat. Commun.* **2014**, *5*, 3585.
[73] S. J. Harris, P. Lu, *J. Phys. Chem. C* **2013**, *117*, 6481.
[74] Y. Kao, M. Tang, N. Meethong, J. Bai, W. C. Carter, Y.-M. Chiang, *Chem. Mater.* **2010**, *22*, 5845.
[75] A. L. D. Kilcoyne, T. Tyliszczak, W. F. Steele, S. Fakra, P. Hitchcock, K. Franck, E. Anderson, B. Harteneck, E. G. Rightor, G. E. Mitchell, A. P. Hitchcock, L. Yang, T. Warwick, H. Ade, *J. Synchrotron Radiat.* **2003**, *10*, 125.